Real Space Multiple Forward Scattering of High Energy Electrons by Light-Atom Structures

Tarik R. Drevon[a], David G. Waterman[a], Eugene Krissinel[a]

[a] *Rutherford Appleton Laboratory, Science and Facilty Technology Council, Harwell Campus, Didcot OX11 0QX,United Kingdom*

Abstract

Due to the strong electron-atom interaction, the kinematic theory of diffraction can not be used to describe the scattering of electrons by an assembly of atoms. Dynamical diffraction need to be taken into account by solving Schrödinger's equation. In this paper, the scattering of high energy electrons by a regular array of light atoms is solved exactly using the T-matrix in spherical coordinates. Using the independent atom model, each atom is represented by a sphere with an effective constant potential. The validity of the forward scattering approximation and the phase grating approximation assumed by the popular multislice method are discussed. An interpretation of multiple scattering is proposed and compared with existing interpretations.

Keywords: High Energy Electron Diffraction, T-matrix

1. Introduction

1.1. Motivation

Since the first experimental demonstration of electron diffraction in 1928, theory of dynamical diffraction has been developed [1, 2]. Besides, multiple scattering [3, 4, 5, 6] In electro nmicroscopy, theories have also been proposed providing an intuitive picture dynamical diffraction to describe channeling in crystals [7]. has also extensively been studied in solid state physics over the 20th century. Studying dynamical theory is unavoidable when it comes to electron-atom interaction, since even at very high electron energies commonly used in modern transmission electron microscopes, the interaction is so strong that the kinematic theory of diffraction is not theoretically valid for crystals thicker than a few nm[8, 9]. In practice, crystal growth cannot be controlled to such a degree of accuracy and nano-crystals of organic compounds are usually on the order of tens to hundreds of nanometers. This is known as a challenging aspect of high energy electron diffraction (HEED) as it should significantly complicate the structure determination process. However, successfull structure determination based on the standard kinematic theory used in X-ray diffraction have regularly been demonstrated over the past 10 years[10, 11] suggesting that dynamical diffraction may not affect the diffraction intensities as much as the theory suggests. Although, dynamical refinement based structure determination [12] usually leads to better intensity predictions [13], the agreement between theory and experiment is still significantly worse than those obtained for X-rays [14]. It is therefore crucial to develop more accurate models of electron diffraction by crystals.

1.2. state of the art

The multislice(MS) [15] and Blochwave(BW) [1] approaches are the most popular methods for simulating scattering of high energy electrons in crystals. The MS is particularly well suited for solving large structures as it involves successive convolutions which can be very efficiently computed with the Fast Fourier Transform(FFT) [16]. To avoid aliasing transverse periodic boundary conditions must be met which is only possible for orthorombic structures in zone axis orientations. Although small beam tilt can also be used [17, 18], simluations with arbitrary orientations must be performed by simulating a full crystal with added zero padding. This can quickly become computationnally challenging.

On the other hand, BW method can simulate small structures in any arbitrary orientations. Although some efficient implementation [19] can simulate moderately large structures, BW cannot be applied to large structures due to the unfavorable scaling behaviour of the matrix diagonalization involved. Non periodic structures, defects and solvent scattering can hardly be modelled either with this method.

Some very efficient implementations are available [20] for convergent beam electron diffraction (CBED) and [21]. Implementations with full modelling capabilities one while computationnally efficient, specifically designed at continuous electron diffraction (CED) of large organic structure would be ideal for macromolecular structure determination.

---

*Corresponding author
Email address: `eugene.krissinel@stfc.ac.uk` (Eugene Krissinel)

The purpose of this paper is to propose an alternative real space approach to the scattering of fast electrons by light-atom structures based on the T-matrix formalism. The T-matrix has been extensively applied to various areas of physics including electromagnetics [22, 23, 24], optics [25] and acoustics [26, 27]. Although not computationnally competitive with multislice for large systems, this approach provides an exact solution to Schrödinger's equation for an assemble of spherically symmetric effective atomic potentials in the independent atom model (IAM). An intuitive understanding of multiple scattering in the forward scattering approximation is presented and compared with existing intepretations. The validity of the forward scattering approximation and the phase grating approximation used by multislice are then discussed. Conclusions are drawn and extensions of this approach to account for incoherent inelastic scattering are outlined.

2. Theory

The problem of the scattering of fast electrons by an assembly of atoms is found by solving Schröodinger's equation :

$$\left[-\frac{\hbar^2}{2m_e}\boldsymbol{\nabla}_{\mathbf{r}}^2 - eV(\mathbf{r}) \right] \Psi = E\Psi \tag{1}$$

where $\hbar$ is plank's constant, m_e the mass of the electron, e the elementary charge, $V(\mathbf{r})$ is the spatially varying electrostatic potential created by the atoms and E the energy of the incident electrons. The wave function is sought as a sum of an incident wave $\Psi^{(i)}$ and a scattered wave $\Psi^{(s)}$.

2.1. T-matrix formulation

In its standard form, the T-matrix solves for the case where the electrostatic potential is uniform constant inside non overlapping spheres and the incident wave is described by a plane wave of wavenumber $k_0 = 2\pi/\lambda$ (optics convention). The setup shown in figure 1. The formulation is well established and the theory is outlined for the purpose of introducing the forward multiple scattering approximation picture.

In each domain, the problem is reduced to Helmholtz's equation in spherical coordinates :

$$\begin{aligned}
\boldsymbol{\nabla}_{\mathbf{r}_p}^2 \Psi + k_p^2\Psi &= 0 \\
k_p &= k_0 n_p \\
k_0 &= \sqrt{\frac{2m_e E}{\hbar^2}} \\
n_p &= \sqrt{1 + \frac{V_p}{E}}
\end{aligned}$$

where $V_p \geq 0$ is the constant attractive potential inside sphere p of radius a_p centered at $\mathbf{d}_p$, k_p the wave number inside the sphere and n_p can be referred to as the refractive
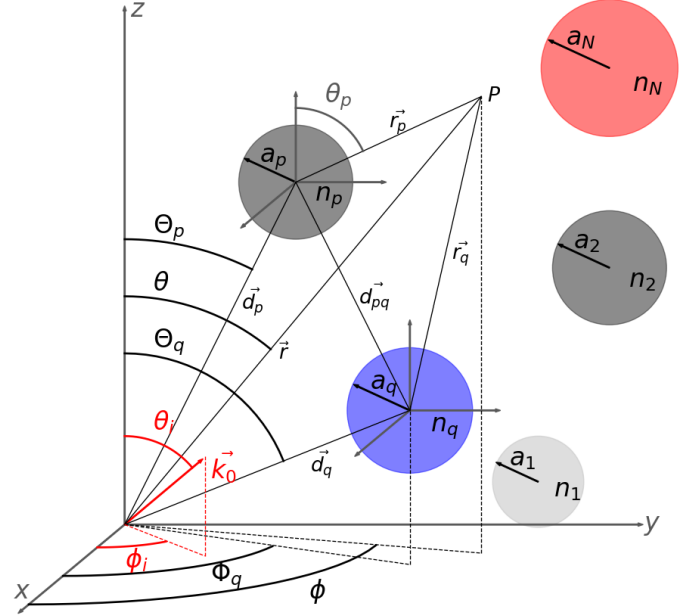

Figure 1: The problem solved by the T-matrix

index by analogy with optics. The scattered wave function inside and outside of sphere p can then be expressed as :

$$\begin{aligned}
\Psi_p^{(in)}(\mathbf{r}_p) &= \sum_{l=0}^{\infty} j_l(k_p r_p) \sum_{m=-l}^{m=l} a_{p;lm} Y_l^m(\theta_p, \phi_p) \\
\Psi_p^{(out)}(\mathbf{r}_p) &= \sum_{l=0}^{\infty} h_l^{(1)}(k_0 r_p) \sum_{m=-l}^{m=l} b_{p;lm} Y_l^m(\theta_p, \phi_p)
\end{aligned}$$

where $p = 1..N$, j_l and $h_l^{(1)}$ are the spherical Bessel and Hankel functions of the first kind, Y_l^m are the spherical harmonics or order l and azimuthal order m. Note that these equations are expressed in the reference frame of each sphere p hence the use of variable $\mathbf{r}_p$.

The unknown coefficients $a_{p;lm}$, $b_{p;lm}$ are found by imposing the continuity of the wave function and its radial derivative at the surface of each sphere p :

$$\begin{aligned}
\left(\sum_{q=1}^{N} \Psi_q^{(out)} + \Psi^{(i)} \right)\Big|_{r_p=a_p} &= \left(\Psi_p^{(in)} \right)\Big|_{r_p=a_p} \\
\partial_{r_p}\left(\sum_{q=1}^{N} \Psi_q^{(out)} + \Psi^{(i)} \right)\Big|_{r_p=a_p} &= \partial_{r_p}\left(\Psi_p^{(in)} \right)\Big|_{r_p=a_p}
\end{aligned}$$

where $f^{(i)}$ is the incident electron wavefunction and a_p the radius of sphere p.

Using the orthogonality of the spherical harmonics the following linear system yields the unknown coefficients :

$$
\begin{aligned}
a_{p;lm} &= u_{p;l}c_{lm} + u_{p;l}\sum_{q\neq p}^{N} \\
&\quad \sum_{\nu=0}^{\infty}\sum_{\mu=-\nu}^{\mu=\nu} a_{\nu,\mu;l,m}^{(out-in)}(\mathbf{d}_{pq})b_{q;\nu\mu} \quad (2)
\end{aligned}
$$

$$
\begin{aligned}
b_{p;lm} &= v_{p;l}c_{lm} + v_{p;l}\sum_{q\neq p}^{N} \\
&\quad \sum_{\nu=0}^{\infty}\sum_{\mu=-\nu}^{\mu=\nu} a_{\nu,\mu;l,m}^{(out-in)}(\mathbf{d}_{pq})b_{q;\nu\mu} \quad (3)
\end{aligned}
$$

where the translational addition theorem[28] has been used to express the field scattered by sphere q in the reference frame of sphere p, formally written as $f_q^{(out)}(\mathbf{r}_p)$. This operation involves the coupling coefficients $a_{\nu,\mu;l,m}^{(out-in)}(\mathbf{d}_{pq})$ where $\mathbf{d}_{pq} = \mathbf{d}_q - \mathbf{d}_p$.

The coefficient c_{lm} are related to the incident wave. In the case of a plane wave $e^{j\mathbf{k}_0\cdot\mathbf{r}}$, $j = \sqrt{-1}$, the addition theorem is used to expand the plane wave on the family basis os Spherical Bessel soluions :

$$
\begin{aligned}
c_{lm} &= 4\pi j^l Y_l^{m*}(\theta_i,\phi_a)\,e_p \\
e_p &= e^{jk_0 d_p \zeta_p} \\
\zeta_p &= \sin(\Theta_p)\sin(\Phi_p)\sin(\theta_i) + \cos(\Theta_p)\cos(\theta_i)
\end{aligned}
$$

where d_p, Θ_p, Φ_p being the spherical coordinates of the centre of sphere p in the global coordinate system, $0 \leq \theta_i \leq \pi$ is the angle of incidence with respect to the $\mathbf{e}_z$ axis, $\phi_i = \pi/2$ since the propagation is in the (y,z) plane and e_p is the phase offset at sphere p. The different notations as illustrated on figure 1.

The coefficients $u_{p;l}$ and $v_{p;l}$ are expressed as :

$$
u_{p;l} = \frac{h_l'(k_0 a_p)j_l(k_0 a_p) - h_l(k_0 a_p)j_l(k_0 a_p)'}{j_l(k_p a_p)h_l'(k_0 a_p) - n_p j_l'(k_p a d_p)h_l(k_0 a_p)}
$$

$$
v_{p;l} = \frac{n_p j_l'(k_p a_p)j_l(k_0 a_p) - j_l(k_p a_p)j_l'(k_0 a_p)}{j_l(k_p a_p)h_l'(k_0 a_p) - n_p j_l'(k_p a_p)h_l(k_0 a_p)}
$$

where $z_l' = \partial_\rho z_l(\rho)$.

Equations (2,3) can be written in a matrix notation :

$$
(\mathbf{I} - \mathbf{T})\mathbf{A} = \mathbf{L} \quad (4)
$$

where $\mathbf{I}$ is the identity matrix, $\mathbf{A}$ is the unknown vector coefficients, $\mathbf{L}$ the incident wave right hand side and $\mathbf{T}$ is the cross-coupling matrix.

2.2. Far field and scattering cross section

In electron crystallography, the diffraction pattern of particular interest which is recorded in the far field. Using

the asymptotic behaviour $h_l^{(1)}(k_0 r_p) \approx (-j)^{l+1}\frac{e^{jk_0 r_p}}{k_0 r_p}$ and since $\theta_p \approx \theta, \phi_p \approx \phi$ the far field scattering amplitude $f_p(\theta,\phi)$ from sphere p can be written as :

$$
f_p(\theta,\phi) = \sum_{l=0}^{\infty}\sum_{m=-l}^{l}(-j)^{l+1}b_{p;lm}Y_l^m(\theta,\phi) \quad (5)
$$

The total scattering amplitude is the sum of the contribution from all individual spheres. Since in the far field, $r_p \approx r - \mathbf{d}_p\cdot\mathbf{e}_r$:

$$
f(\theta,\phi) = \sum_{p=1}^{N}f_p(\theta,\phi)e^{-jk_0\mathbf{e}_r\cdot\mathbf{d}_p} \quad (6)
$$

The normalized differential scattering cross section is defined as :

$$
\frac{\sigma(\theta,\phi)}{\pi a_p^2} = \frac{4\pi r^2}{\pi a_p^2}\left\|\frac{\Psi^{(s)}(r,\theta,\phi)|}{\Psi^{(i)}(r,\theta,\phi)}\right\|^2 = \frac{4|f(\theta,\phi)|^2}{(k_0 a_p)^2} \quad (7)
$$

where we have used $\Psi^{(s)}(r,\theta,\phi) \underset{r\to\infty}{\approx} \frac{e^{jk_0 r}}{k_0 r}f(\theta,\phi)$.

3. Real space forward multiple scattering picture

3.1. T-matrix forward multiple scattering approximations

Expression (4) is a convenient way to write the system as it readily identifies $\mathbf{L}$ as the solution to the uncoupled problem. Indeed, $a_{p;lm} = c_{lm}u_{p;l}$, $b_{p;lm} = c_{lm}v_{p;l}$ are them well known analytical solutions of Mie scattering by a soft sphere.

The cross-coupling matrix $\mathbf{T}$ accounts for multiple scattering effects. If $\mathbf{A}$ is written $\mathbf{A} = (..a_{p;lm}, b_{p;lm}...)^T$, $\square^T$ denoting transposition, then $\mathbf{T}$ is block diagonal :

$$
\mathbf{T} = \begin{bmatrix}
\mathbf{0} & ..\,\mathbf{T}_{1q}\,.. & ..\,\mathbf{T}_{1p}\,.. & \mathbf{T}_{1N} \\
\mathbf{T}_{q1} & ..\,\mathbf{0}\,.. & ..\,\mathbf{T}_{qp}\,.. & \mathbf{T}_{qN} \\
\mathbf{T}_{p1} & ..\,\mathbf{T}_{pq}\,.. & ..\,\mathbf{0}\,.. & \mathbf{T}_{pN} \\
\mathbf{T}_{N1} & ..\,\mathbf{T}_{Nq}\,.. & ..\,\mathbf{T}_{Np}\,.. & \mathbf{0}
\end{bmatrix}
$$

where $\mathbf{T}_{pq}$ represents the scattering from sphere p due to the scattering from sphere q. If the problem is fully coupled, the scattering from sphere p affects scattering from sphere q and vice versa which therefore requires inversion of the system.

As detailed further down below, backscattering can be neglected for very fast electrons which is known as forward scattering approximation. This results in $\mathbf{T}$ begin lower triangular if the spheres are sorted in ascending order along $\mathbf{e}_z$. Inversion is therefore no longer necessary and calculations can be performed sequentially one atom after the other.

Since $\mathbf{A}_0 = \mathbf{L}$ represents single scattering, we can establish that $\mathbf{A}_1 = \mathbf{T}\mathbf{A}_0$ accounts for secondary scattering.
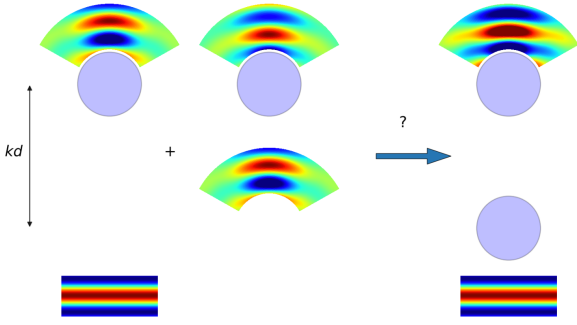
Figure 2: Two-level forward scattering approximation using the T-matrix approach. Neglecting backscattering, scattering from the second scatterer located at distance kd from the first scatterer can be approximated by the sum of 1) the kinematic scattering to the incident beam and 2) the secondary scattering in response to the kinematic scattering from the first scatterer.

Similarly, outward scattering ampltiudes from sphere p can be written :

$$
\begin{aligned}
\mathbf{b}_p &= \mathbf{b}_p^{(0)} + \sum_{q,z_q<z_p} \mathbf{T}_{pq}\mathbf{b}_q^{(0)} \\
&\quad + \mathbf{T}_{pq}\sum_{q,z_q<z_p}\mathbf{T}_{qr}\sum_{r,z_r<z_q}\mathbf{b}_r^{(0)} + .. \\
&= \sum_{n=0}\mathbf{T}^n\mathbf{b}_p^{(0)} = \sum_{n=1}\mathbf{b}_p^{(n)}
\end{aligned}
\tag{8}
$$

where the first term accounts for kinematic scattering, the second term for secondary scattering, the third term three time scattering and so on. This is a similar development to the Korringa-Kohn-Rostoker (KKR) theory of multiple scattering [3, 4, 5]. This forward multiple scattering picture in the case of a 2 body problem is illustrated in figure 2. From a compuational point of view, (8) may offer an advantage over the full forward scattering approximation if only a few n-time scattering terms are necessary. Indeed, since each term in the expansion depend on precomputed coefficients $b_{p;lm}^{(0)}$, the $b_{p;lm}^{(n)}$ coefficients for the n-time scattering term can be massively parallelized for each atom.

3.2. Scattering probabilties

The probabiliy of an electron to be scattered elastically n times can be estimated classically from ballistic arguments using a continuous model of matter. It can be established [29] that the probabilty of an electron to be elastically scattered n times after passing through an amorphous sample of thickness z follows a Poisson distribution statistics $P_e^n = \frac{1}{n!}(z/l_e)^n e^{-z/l_e}$ where l_e is the elastic mean free path.

We may use the scattering cross section to define the probability of an electron being scattered. If S is the area over which the specimen is illuminated and z the thickness of the specimen, the incident plane wave can be normalized by $|A|^2 = 1/Sz$. The flow of electrons per unit time

per unit area [30] is then $J_0 = \hbar k_0/m|A|^2 = v_0/Sz$ where v_0 is the speed of the incident electron and J_0S is the number of electron illuminating the specimen per second. Besides, by definition $J_0\sigma$ is the number of electrons scattered per second and it takes $\Delta t = z/v_0$ for an electron to go through the specimen, so that $\sigma J_0 z/v_0$ is the probability of an electron to be scattered. Therefore :

$$
P_{scat} = \frac{\sigma}{S}
$$

where S can be seen as the surface illuminated in selected area electron diffraction (SAED). When performing a multislice simulation, S is the area of the simulated domain (transverse super cell if performing a periodic simulation).

Let's define f_n the scattering amplitudes obtained by computing scattering from the wave being scattered n times. It can readily be established that :

$$
\begin{aligned}
f(\theta) &= \sum_{n=1}^{N} f_n(\theta) \\
\sigma &= \sum_{n=1}^{N} \sigma_n \\
\sigma_n &= |f_n|^2 + 2\Re f_n \sum_{m>n}^{N} f_m^*
\end{aligned}
\tag{9}
$$

where $P_n = \sigma_n/S$ can be defined as the probability of an electron to be scattered n times. Since contributions from multiple scattering terms should normally be in ascending order, this definition ensures that the probability of scattering of order n increases as soon as the corresponding term m-times scattering start contributing to the scattering amplitudes.

The probability of an electron to not being scattered is naturally $P_{coh} = 1 - P_{scat}$. For an very large number N of scatterers regularly spaced by distance dz, using the average cross section $\sigma_a = \sigma/N$, the average scattering probability to be scattered over distance dz would be $P(dz) = \sigma_a\rho dz = dz/l_e$ where $\rho = 1/Sdz$ is the density since since Sdz contains only one scatterer and $l_e = 1/\sigma_a\rho$ is the mean free path. This is consistent with [31].

3.3. First Born approximation and kinematic scattering

Assuming normal incidence $\theta_i = 0$ so that $e_p = e^{jk_0 d_p}$ and noting that the Ewald sphere can be represented by $\mathbf{q} = K(\sin\theta\cos\phi, \sin\theta\sin\phi, 1-\cos\theta)$ in transfer vector momentum space, $K = 1/\lambda$ begin the wave number in crystallographic convention, keeping only the kinematic term in (8) and injecting in the far field (6) gives :

$$
f(\theta,\phi) = \sum_{p=1}^{N} f_p^{(e)} e^{2j\pi\mathbf{q}\cdot\mathbf{d}_p}
\tag{10}
$$

where $f_p^{(e)}$ is the scattering amplitude of sphere p in the First Born approximation also known as the form factor. Equation (10) does correspond to the standard kinematic formula for the structure factor traditionnally used

in crystallography. Note that the kinematic approximatio is nothing less than the first first Born approximation applied to the whole assembly of atoms. It will be seen further down below that it is possible for the first Born approximation to hold at the scatterer level while being invalid at the assembly level.

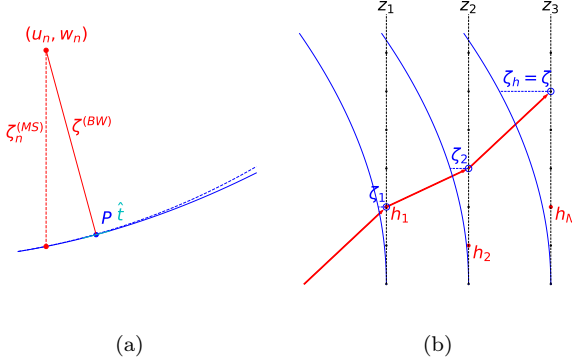### 3.4. Multiple scattering in multislice

(a)   (b)

Figure 3: Multiple scattering in multislice. a) Distance $\zeta^{(MS)}$ to the Ewald paraboloid(solid curve) as approximated by multislice and distance $\zeta^{(BW)}$ to the Ewald sphere(dashed curve) known as the excitation error in the blochwave theory. Point P is the projection of reciprocal point (u_n, w_n) onto the Ewald parabola. b) Multiple scattering in reciprocal space for $N = 3$ slices located at z_1, z_2, z_3. The beam is scattered by $(h_1, 0)$, then $(h_2, 0)$ and then $(h_N, 0)$ which results in an overall contribution to reflection h on the diffraction pattern. The open blue circles show the subsequent excitation errors $\zeta^{(i)}$.

In multislice, the forward scattering approximation is used and the potential discretized in slices which are propagated from one slice to the other using Fresnel propagator.

A multiple scattering interpretation by the multislice has been proposed [15] which, although analgous to the one presented above, differs in that it is stated in reciprocal space. The expression for the scattering ampltiude $f(h, k)$ of beam h, k is proportional to the following expression :

$$f(h, k) \propto \sum_l \sum_{h_1} \sum_{k_1} \sum_{l_1} \cdots \sum_{h_{N-1}} \sum_{k_{N-1}} \sum_{l_{N-1}} Q_{h_1, k_1, l_1} \cdots$$
$$Q_{h_{N-1}, k_{N-1}, l_{N-1}} Q\Big(h - h_u, k - k_v, l - l_w\Big)$$
$$e^{-2\pi j\big(H\zeta - \Delta z \sum_{n=1}^{N-1} \zeta_n\big)} \tag{11}$$

where $h = \sum_{n=1}^{N} h_n$, $k = \sum_{n=1}^{N} k_n$, $h_u = \sum_{n=1}^{N-1} h_n$, $k_v = \sum_{n=1}^{N-1} k_n$, $l_w = \sum_{n=1}^{N-1} l_n$, $H = N\Delta z$ is the total thickness of the sample, N the number of slices of thickness Δz, $Q_{h,k,l} = -j/\Delta z \delta_{h,k} e^{-2j\pi l_n z_n/c} + \sigma F_{h,k,l}$, $F_{h,k,l}$ is the structure factor, $\sigma = 2\pi m_e h/\lambda$ the interaction parameter, ζ the excitation error of beam (h, k, l) and ζ_n is the excitation error of beam $(\sum_{r=1}^{n} h_r, \sum_{r=1}^{n} l_r)$. The excitation error is exprred as :

$$\zeta = \frac{1}{2K}\left(\frac{h}{a^2} + \frac{k}{b^2}\right) - \frac{l}{c} \tag{12}$$

where a, b and c are the lattice constants of the crystal and $K = 1/\lambda$ the wave number. Equation (12) is the longitudinal distance of beam (h, k, l) to the paraboloid shown in figure 3a. This paraboloid is a very accurate representation of the Ewald sphere for large wave number K. ζ is therefore very close to the excitation error commonly defined in crystallography.

From equation (11) it is possible to gather terms in powers of $Q_{0,0,0}^{N-n}$ into $f_{h,k}^{(n)}$ which corresponds to the incident beam scattered n times before contributin to reflection h, k. The term $Q_{0,0,0}^{N}$ only appears for $h = k = 0$ and corresponds to the unscattered direct beam. There are N terms involving $Q_{0,0,0}^{N-1}$ depending on which slice the single scattering event took place. There are $N(N-1)/2$ terms involving $Q_{0,0,0}^{N-2}$ depending on which pair of slices are considered the two level scattering process and so on. This multiple scattering picture is illustrated in 2D in figure 3b for a case with $N = 3$ and using only beams in the zero order Laue zone (ZOLZ) $l_i = 0$.

Using only ZOLZ beams, $f_{h,k}^{(1)}$, $(h, k) \neq (0, 0)$ is expanded as :

$$f_{h,k}^{(1)} \propto F_{h,k,0} \sum_{m=1}^{N} e^{-2j\pi m \Delta z \zeta} \tag{13}$$

which is the well known kinematic scattering regime where the sum converges to the standard Ewald sphere curvature factor $\sin(\pi\zeta H)/\pi\zeta$ for infinitely thick slices $N \to \infty, \Delta z \to 0$, $N\Delta z = H$

For a 2 level scattering using only ZOLZ beams, $f_h^{(2)}$ would expanded as (written in 2D here) :

$$f_h^{(2)} \propto \sum_{h_1} F_{h_1,0} F_{h-h_1,0}$$
$$\sum_{m_1=1}^{N} \sum_{m_2>m_1}^{N} e^{-2j\pi\Delta z\big(m_1\zeta_1 + m_2(\zeta - \zeta_1)\big)} \tag{14}$$

4. Application and Results

Although very efficient open source implementations are available for electromagnetics [32, 33], an implementation suited for solving Schrödinger's equation has been made available [34].

In practice, the sums over (2,3) have to be truncated to a maximum integer order l_{max}. A rule to obtain accurate results is to take l_{max} a few integer above the maximum value of ka since the spherical Bessel functions of order l have enough ripples to capture the periodicity of the incident wave in the vicinity of the sphere. Moreover, the translational addition theorem provides an approximation of the spherical Hankel functions with decreasing accuracy from the center at which it is written similarly to a Taylor's expansion. This is illustrated in figure 4a where the error between $h_l^{(1)} Y_{lm}$ for $l = 4$ and $m = 2$ computed at the origin and using the translational addition theorem
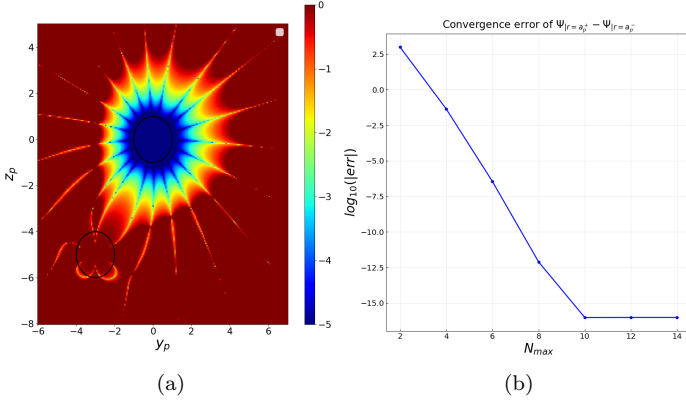
Figure 4: a) Error between $h_l^{(1)} Y_{lm}$ for $l = 4$ and $m = 2$ computed at the origin and using the translational addition theorem $\mathbf{d}_p = (0, 3, 5)$ with $\nu_{max} = 10$. The circle represent spheres of radius 1. Color axis in logscale. b) Continuity error at the sphere boundaries in the T-matrix with increasing order. For this example $N = 4$ and $ka_{max} = 4$.

with $\mathbf{d}_p = (0, 3, 5)$ and $\nu_{max} = 10$ is displayed in logscale. This allows for distances between spheres to be arbitrarily large. The criteria for selecting l_{max} is best evaluated by assessing the continuity of the wave functions at the sphere boundaries as shown in figure 4 for $N = 4$ and $ka_{max} = 4$. This is also used to validate the correctness of the implementation since it can be seen that machine accuracy can be reached when increasing the order.

4.1. Validity of forward scattering and phase grating approximations for light atoms

In the case of very fast electrons typically used in transmission electron microscopes $E = 50 - 300 keV$. Inclusion of relativistic effects result in $\lambda = 0.025 \text{Å} @ 200 keV$ which will be assumed from now on unless stated otherwise.

In the IAM, the Coulomb potential is created by the charge of the nucleus and its electron cloud. It is fitted with a sum of 3 screened Coulomb potential and 3 Gaussian terms [35]. For typical light atoms such as commonly found in organic compounds, a single screend Coulomb potential term can be a pretty good approximation as shown in figure 5a. The solution to Schrödinger's equation in such a potential can only be solved perturbatively [36] and is beyond the scope of this document. However, indicative values for k_p and ka_p can be used with a multi-shell representation as shown as blue patches on figure 5a. Although the range of the screened Coulomb potential is theoretically infinite, it can reliably be truncated to radius ka. In figure 5b the multi-shell scattering amplitudes in the Born approximation are shown for increasing values of truncation radius. A satisfactory agreement with the electron diffraction scattering factors is obtained for normalized raidus as large as $ka = 350$ to account for the proper low angle representation although the potential is very small at such radius.

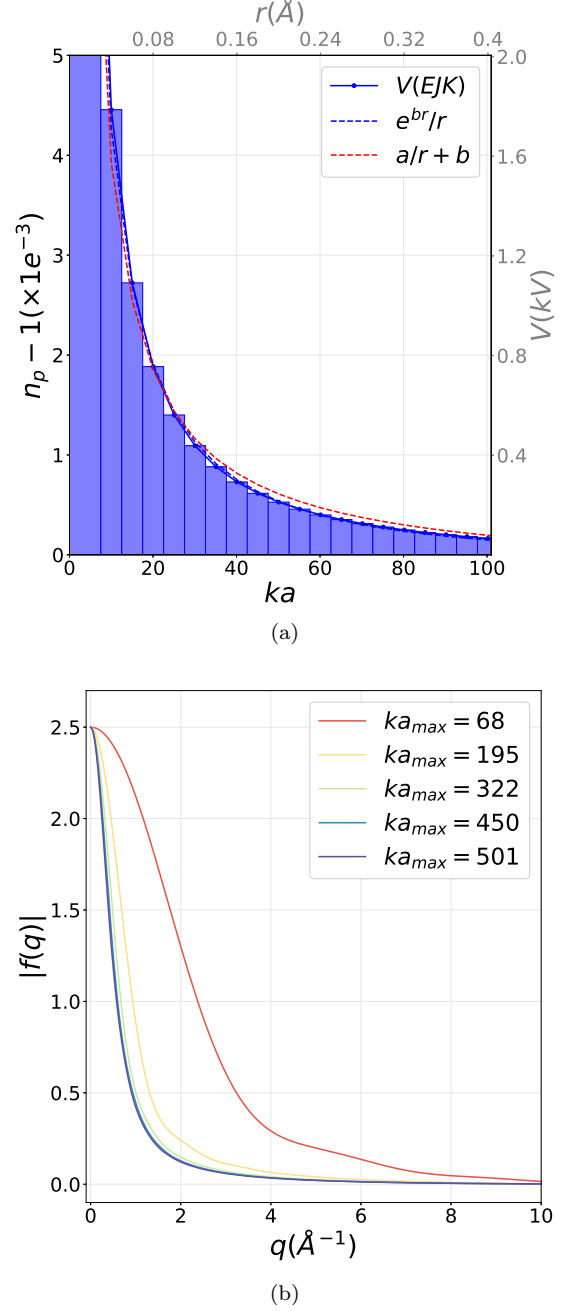As mentioned above, such large radius would be quite

(a)

(b)

Figure 5: a) Electrostatic potential created by an atom of carbone with the IAM (blue solid line), fitted single screened coulomb potential (blue dahsed line), fitted Coulomb potential with offset (red dashed line). The blue patches show a multi-shell approximation model which can be used to represent the potential using a T-matrix approach. b) Scattering amplitude in the Born approximation for the multi-shell model with increasing truncation radius ka_{max}. The electron form factors factors is shown as dashed line.

hard to simulate with the T-matrix due to the large orders to be included. However, the medium radius range should provide a reasonable picture of dynamical scattering. Figure 6a shows the total scattering cross section of a single sphere with increasing radius for a range of values of n_p. The dark blue curve shows the locations of the spherical
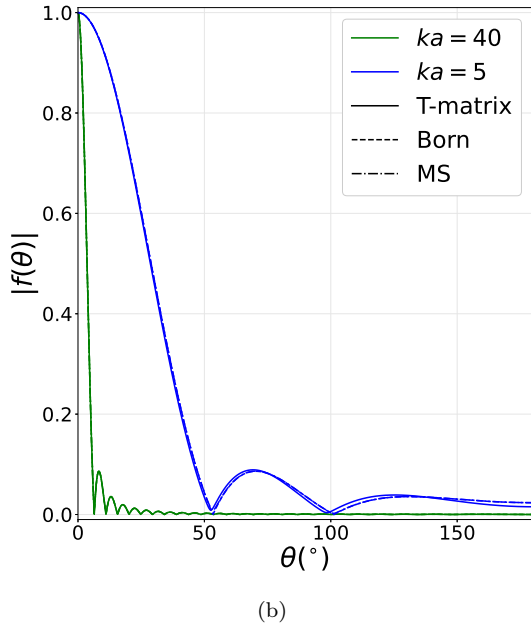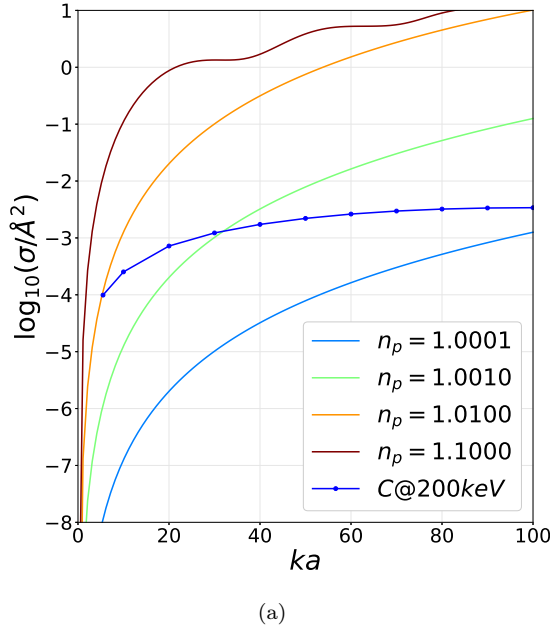
(a)

(b)

Figure 6: a) Total scattering cross section σ at $200keV$ for a few values of n_p over a range of normalized radius ka. The dark blue curve shows the location of the carbone spherical shells . b) Shape of the scattering amplitude for normalized radius $ka = 5$, $n_p = 1.025$ (blue) and $ka = 40$, $n_p = 1.001$(green). Also shown, the Born approximation (dashed lines) and the phase grating approximation used in multislice (dash-dotted lines).

shell for Carbone. It becomes almost flat from $ka = 30$, $n_p = 1.001$ although slightly keeps increasing to reach the asymptotic value $\sigma \approx 0.0035\text{Å}^2$ which is almost identical to the average elastic cross section for real carbon in the Born approximation [31]. Figure 6b shows the shape of the far field amplitudes for 2 parameter sets of ka,n_p indicative of Carbone shells. The Born approximation captures

very well the shape for both sets although some minor differences appear at large angles for $ka = 5$, $n_p = 1.025$ The phase grating approximation provide some improvement at low angles.
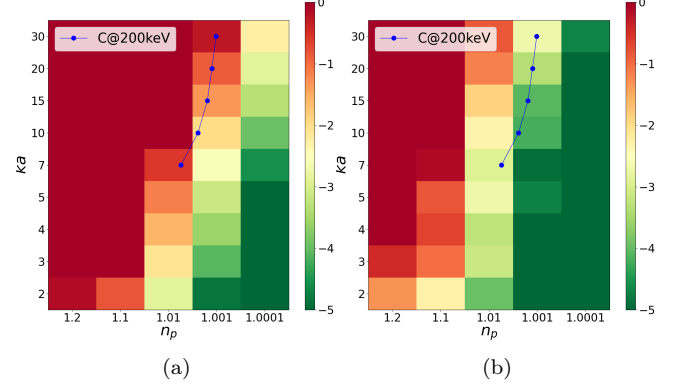

(a)   (b)

Figure 7: (ka, k_p) map(color axis in logscale) of the error of $b_{p;lm}$ for a 2 scatterer system using the a) Kinematic scattering approximation. b) Forward scattering approximation. The blue dot correspond to the location of the spherical shells of Carbone atom at $E = 200keV$.

Figure 7a and 7b show for a 2 body problem the error in a (ka, n_p) map in computing the coefficients $err(b_{p;l,m}) = \sum_{p;l,m} |b_{p;l,m} - b_{p;l,m}^{approx}|)$ as a result of using the kinematic and forward approximations respectively. For this case an value of $kd = 3ka$ is used which should represent interatomic distances. Overall it is very clear that the forward scattering approximation is very accurate over all range of parameter sets for carbone which is expected since there is very little back backscattering beyond $90°$. On the other hand the kinematic approximation does not appear quite as good even for this mere 2 dody problem. Although not shown here, both the kinematic and forward scattering approximation tend to work slightly better with increasing distances kd since coupling between the the spheres is reduced. It is therefore less likely to affect scattering from the other spheres. The low values of n_p result in overall good approximation of both the uncoupled and forward scattering approximation. This is an anticipated result since for weak potentials, the kinematic approximation is more valid. The uncoupled approximation improves with small radii since Small ka result in small scattering cross section, On the other hand the forward scattering approximation improves with larger values of ka since backward scattering is less likely for large ka.

Figure 8a shows the scattering coefficients $b_{p;l,m}$ in complex space for a this 2 body problem where $n_p = 1.01$, $kd = 3ka$ while increasing radius ka (up to $ka = 15$) for a selected set of orders l. Only the coefficients for sphere $p = 2$ are shown since it is the mostly affected sphere by the approximations. Only $m = 0$ coefficients are used since under planar illumination this configuration has azimuthal symmetry. The coefficients are computed using the full T-matrix, the forward scattering approximation
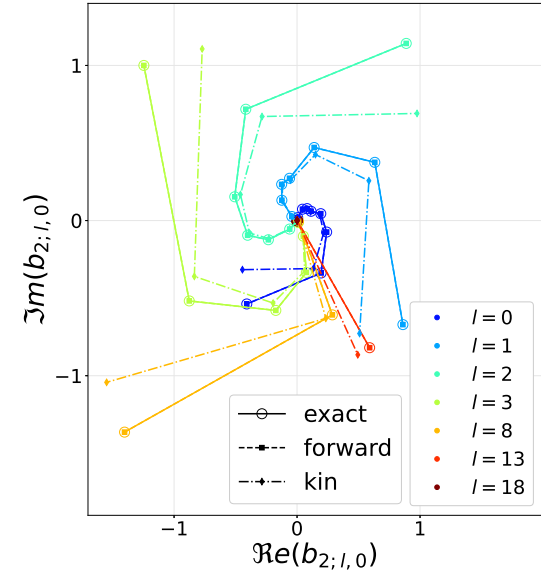
(a)
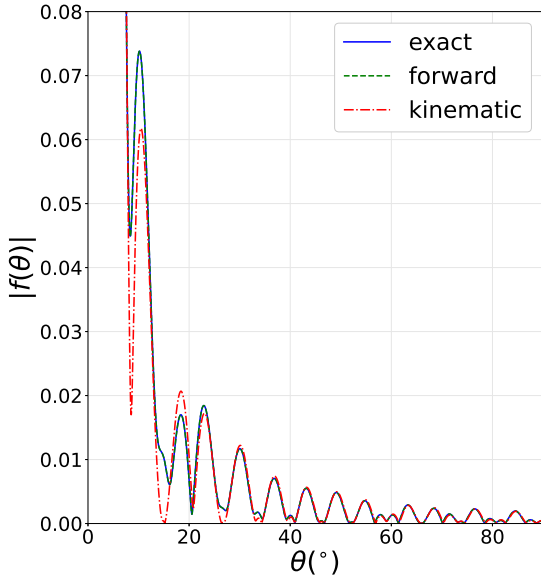
(b)

Figure 8: a) Complex space scattering coefficients $b_{p;l,m}$ for a 2 body problem for $n_p = 1.01$, $kd = 3ka$ with increasing radius ka. Only the coefficients for sphere $p = 2$ and $m = 0$ are shown. The coefficients were computed from full T-matrix (open circles), the forward scattering approximation (squares) and the kinematic approximation (diamonds). b) Comparison of far field scattering amplitudes for $N = 2$, $ka = 30$, $n_p = 1.01$, $kd = 2ka$ using full T-matrix (solid blue), forward approximation(green dashed) and kinematic approximation (red dashed-dotted).

and the kinematic approximation. In order to get this spiralling galaxy picture, the coefficients where divided by the phase factor at sphere p, i.e. $b_{p;lm}e^{jkd}$. The arms of the galaxy are rotated by $\pi/2$ from one order to the other as a result of the j^l factor in the spherical expansion of the

incident plane wave. All the coefficients increase with ka as a result of the increasing scattering cross section with ka. For a given ka, the strongest is contributing orders are around $l = ka$ as a direct manifestation of the convergence behaviour presented above. It can be observed that the kinematic approximation error increases with the radius while the forward approximation is very accurate across all radius.

Figure 8b shows a comparison of the computed far field scattering amplitudes for $N = 2$, $ka = 30$, $n_p = 1.01$, $kd = 2ka$ using the full T-matrix, the forward approximation and the kinematic approximation. The peaks and valleys are both due to the single scattering profile of the constant sphere and the interferometric path length e^{jkd}. It is already possible to notice that the coupled problem as a slight average effect ove the kinematic pattern, a well known feature of dynamical diffraction.
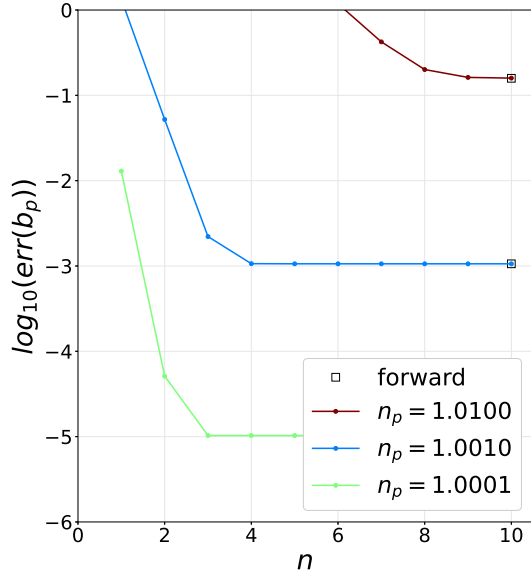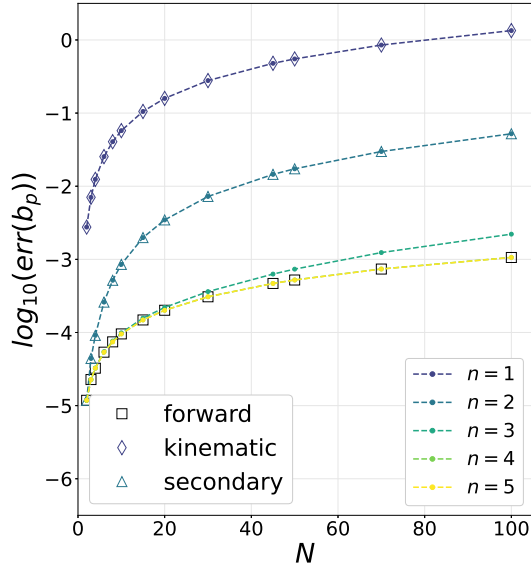
4.2. Successive multiple scattering approximations

Finally, we consider an array of N identical scatterers regularly spaced by $kd = 3ka$ under normal illumination and consider the successive multiple scattering approach. This is an extreme channelling case where dynamical scattering is anticipated to be strong.

Figure 9a and 9b show the evolution of the error on scattering amplitude coefficients for an increasing number of spheres while also varying the number of successive approximations. for a fixed parameter set $ka = 7$, $kdka = 3$. The forward scattering approximation becomes worse and worse for increasing numbers of spheres as a result of accumulated errors. This is limitation of a forward scheme such as the one performed by multislice which is only accurate up to a certain simulated thickness. Overall the successive approximation schemes naturally converge to the forward approximation for sufficiently large n. However, more orders need to be included as the number of spheres (or thickness) increases. This is similar to other multiple scattering approaches. For example, in the case of a 2 beam configuration, it was shown [?] that the scattered beam could be expressed using expansion 11 considering only the scattering terms of the the primary beam $n = 1, 3, 5...$ The famous 2-beam analytical scattering expression is obtained as the sum of the infinite series.

Figure 10a shows the scattering probabilities of n times scattering for $ka = 7$, $n_p = 1.01$, $ka = 3kd$ with increasing N. The dynamic scattering probably $P_{dyn} = \sum_{n>1} P_n$ and the kinematic probability as well as the total scattering probabilties are shown. It seems that all multiple scattering terms increase with number of spheres in contrast to the ballistic picture of the Poisson distribution [] also shown as dashed-dotted lines using the average scattering cross section. The main reason for this is that the ballistic picture ignores the effect of interference which drastically affects the overall scattering process.

Figure 10b shows the scattering amplitudes f_n associated with n times scattering for $ka = 7$, $n_p = 1.01$ and $N = 15$. The scattering amplitudes have similar shapes
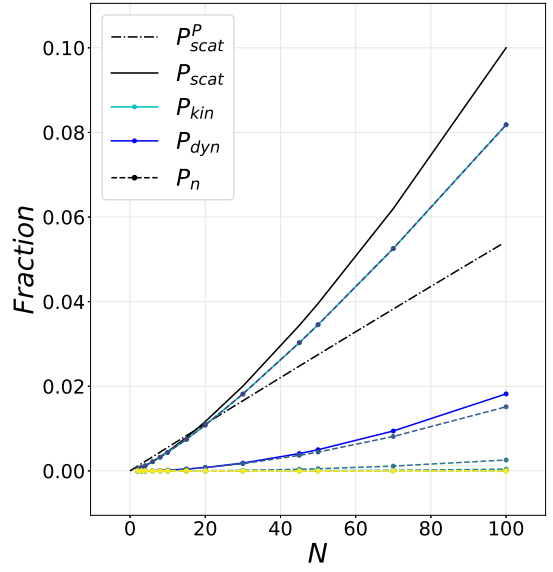
(b)

Figure 9: a) Error on the scattering amplitudes coefficients with increasing number of spheres N for $ka = 7$, $n_p = 1.001$, $kdka = 3$. The forward (squares), kinematic(diamonds) and secondary (triangles) approximations are shown as well as the successive n times multiple scattering approximations (colored dashed lines). b) Error on the scattering amplitudes coefficients with increasing successive approximations for $ka = 7$, $kdka = 3$ and $N = 100$ spheres while varying n_p.
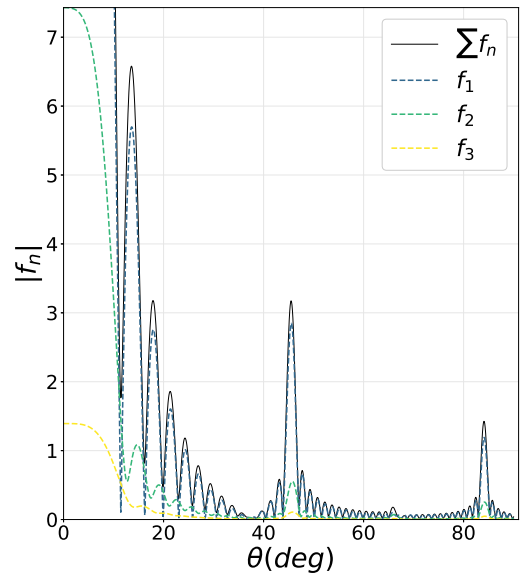

(b)

Figure 10: a) Scattering probabilities (dashed colored lines) of n times scattering, kinematic(cyan solid line), dynamic scattering(blue solid line) and total scattering (black solid) probabilties. The total scattering probabilty following the Poisson distribution using the average scattering cross section is shown as dashed-dotted line. Probabilties have been integrated over angular distribution. Values were $ka = 7$, $n_p = 1.01$, $ka = 3kd$. b) scattering amplitudes f_n associated with n times scattering for $ka = 7$, $n_p = 1.01$ and $N = 15$. The total scattering ampltiude $f = \sum_n f_n$ is shown in solid black.

which mostly contrbitutes to constructive interference although sligth peak misalgnements can be seen.

5. Conclusion and perspective

An alternative approach based on the T-matrix has been applied to the scattering of fast electrons by light-

atom structures. The validity of important approximations used in multislice has been discussed and a multiple scattering approximation framework has been proposed and compared to other existing interpretations.

Although the spherically symmetric effective potential

does not accurately model the potential used in atoms, it was shown that the multiple scattering interpretation should equally apply to the more accurate case of a screened Coulomb potential. A possible inclusion of such a potential could be performed by using a basis of radial functions solutions the Schrödinger's equation in a Yukawa potential such as produced by a variational or other numerical approach. Since the T-matrix mainly relies on the spherical symmetry of the individual scatterers, it can be adapted to any radial family of functions provided translational coefficients can be computed numerically. The main ultimate limitation of both this approach and the traditional multislice lies in the use of the independent atom model which by definition ignores the effect of bonding. While the multislice can be adapted at a computational cost to bonding models such as Transferrable Aspherical Atom Model (TAAM), the T-matrix presented here certainly cannot. However, it is still an open question whether such bonding play an important role in HEED structure determination of organic structures.

The advantage of a multiple scattering approximation approach is that it offers both the possibility of a massively parallel computation of dynamical diffraction while including incoherent inelastic scattering with a stochastic approach. It is indeed strongly anticipated that inelastic scattering has a dramatic mitigation effect of dynamical diffraction even when energy filters are used. This aspect is currently under investigation.

References

[1] H. Bethe, Theorie der Beugung von Elektronen an Kristallen, Annalen der Physik 392 (17) (1928) 55–129. doi:10.1002/andp.19283921704.

[2] J. M. Cowley, Diffraction Physics, 2544.

[3] J. Korringa, On the calculation of the nergy of bloch wave in a metal, Physica 6-7 (1947) 392–400.

[4] W. Kohn, N. Rostoker, Solution of the schrödinger equation in periodic lattices with an application to metallic lithium, Physical Review 94 (5) (1954) 1111–1120. doi:10.1103/PhysRev.94.1111.

[5] J. Korringa, Early history of multiple scattering theory for ordered systems, Physics Reports 238 (6) (1994) 341–360. doi:10.1016/0370-1573(94)90122-8.

[6] P. H. Dederichs, Dynamical diffraction theory, kernforschungsanglage (September).

[7] VanDyck, Simple intuitive theory for diffraction (1996).

[8] R. M. Glaeser, K. H. Downing, High-resolution electron crystallography of protein molecules, ultramicroscopy 52 (1993) 478–486.

[9] G. Subramanian, S. Basu, H. Liu, J.-m. Zuo, J. C. Spence, Solving protein nanocrystals by cryo-EM diffraction : Multiple scattering artifacts, Ultramicroscopy 148 (2015) 87–93.

doi:10.1016/j.ultramic.2014.08.013. URL http://dx.doi.org/10.1016/j.ultramic.2014.08.013

[10] B. L. Nannenga, D. Shi, A. G. W. Leslie, T. Gonen, High-resolution structure determination by continuous-rotation data collection in MicroED, Nature Methods 11 (9) (2014) 927–931. doi:10.1038/nmeth.3043.

[11] B. L. Nannenga, T. Gonen, The cryo-EM method microcrystal electron diffraction (MicroED), Nature Methods 16 (May) (2019) 369–379. doi:10.1038/s41592-019-0395-x. URL http://dx.doi.org/10.1038/s41592-019-0395-x

[12] L. Palatinus, D. Jacob, P. Cuvillier, M. Klementová, W. Sinkler, L. D. Marks, Structure refinement from precession electron diffraction data, Acta Crystallographica Section A: Foundations of Crystallography 69 (2) (2013) 171–188. doi:10.1107/S010876731204946X.

[13] M. Gemmi, E. Mugnaioli, T. E. Gorelik, U. Kolb, L. Palatinus, P. Boullay, S. Hovmoller, J. P. Abrahams, 3D Electron Diffraction : The Nanocrystallography Revolution, ACS Central Sciencedoi:10.1021/acscentsci.9b00394.

[14] P. Oleynikov, S. Hovmöller, X. D. Zou, Precession electron diffraction: Observed and calculated intensities, Ultramicroscopy 107 (6-7) (2007) 523–533. doi:10.1016/j.ultramic.2006.04.032.

[15] J. M. Cowley, A. F. Moodie, The scattering of electrons by atoms and crystals. I. A new theoretical approach, Acta Crystallographica 10 (10) (1957) 609–619. doi:10.1107/s0365110x57002194.

[16] K. Ishizuka, N. Uyeda, A new theoretical and practical approach to the multislice method, Acta Crystallographica Section A: Foundations of Crystallography 33 (5) (1977) 740–749. doi:10.1107/S0567739477001879.

[17] K. Ishizuka, Multislice formula for inclined illumination, Acta Crystallographica Section A: Foundations of Crystallography 38 (6) (1982) 773–779. doi:10.1107/S0567739482001594.

[18] J. H. Chen, D. Van Dyck, M. Op De Beeck, Multislice Method for Large Beam Tilt with Application to HOLZ Effects in Triclinic and Monoclinic Crystals, Acta Crystallographica Section A: Foundations of Crystallography 53 (5) (1997) 576–589. doi:10.1107/S0108767397005539.

[19] J. M. Zuo, A. L. Weickenmeier, On the beam selection and convergence in the Bloch-wave method, Ultramicroscopy 57 (4) (1995) 375–383. doi:10.1016/0304-3991(94)00190-X.

[20] C. Ophus, A fast image simulation algorithm for scanning transmission electron microscopy, Advanced Structural and Chemical Imaging 3 (1) (2017) 1–11. arXiv:1702.01904, doi:10.1186/s40679-017-0046-1.

[21] L. J. Allen, A. J. D'Alfonso, S. D. Findlay, Modelling the inelastic scattering of fast electrons, Ultramicroscopy 151 (2015) 11–22. doi:10.1016/j.ultramic.2014.10.011. URL http://dx.doi.org/10.1016/j.ultramic.2014.10.011

[22] A.-K. Hamid, I. R. Ciric, M. Hamid, Multiple scattering by a linear array of conducting spheres, Canadian Journal of Physics 68 (10) (1990) 1157–1165. doi:10.1139/p90-163.

[23] A.-K. Hamid, I. R. Ciric, M. Hamid, Electromagnetic scattering by an arbitrary configuration of dielectric spheres, Canadian Journal of Physics (68) (1990) 1419–1428.

[24] J. A. Eremin, N. V. Orlov, V. I. Rozenberg, Multiple electromagnetic scattering by a linear array of electrified raindrops, Journal of Atmospheric and Terrestrial Physics 57 (3) (1995) 311–319. doi:10.1016/0021-9169(94)P4361-2.

[25] O. Moine, B. Stout, Optical force calculations in arbitrary beams by use of the vector addition theorem, Journal of the Optical Society of America B 22 (8) (2005) 1620. doi:10.1364/josab.22.001620.

[26] G. T. Silva, A. L. Baggio, J. H. Lopes, F. G. Mitri, Exact computations of the acoustic radiation force on a sphere using the translational addition theorem, Arxiv (2012) 1–8arXiv:1210.2116. URL http://arxiv.org/abs/1210.2116

[27] O. A. Godin, Scattering of a spherical wave by a small sphere: An elementary solution, The Journal of the Acoustical Society of

America 130 (4) (2011) EL135–EL141. doi:10.1121/1.3629140.

[28] T. J. Dufva, J. Sarvas, J. C. Sten, Unified derivation of the translational addition theorems for the spherical scalar and vector wave functions, Progress In Electromagnetics Research B 4 (2008) 79–99. doi:10.2528/pierb07121203.

[29] R. Egerton, Chap3 Physics of Electron Scattering, in: Electron Energy-Loss Spectroscopy in the Electron Microscope, 2011. doi:10.1007/978-1-4419-9583-4.

[30] B. Vainshtein, Chap3 Intensities of Reflections, in: Structure Analysis by Electron Diffraction, 1964, pp. 114–204. doi:10.1016/b978-0-08-010241-2.50008-0.

[31] T. Latychevskaia, J. P. Abrahams, Inelastic scattering and solvent scattering reduce dynamical diffraction in biological crystals, Acta Crystallographica Section B: Structural Science, Crystal Engineering and Materials 75 (2019) 523–531. doi:10.1107/S2052520619009661.

[32] A. Egel, L. Pattelli, G. Mazzamuto, D. S. Wiersma, U. Lemmer, CELES: CUDA-accelerated simulation of electromagnetic scattering by large ensembles of spheres, Journal of Quantitative Spectroscopy and Radiative Transfer 199 (2017) 103–110. arXiv:1706.02145, doi:10.1016/j.jqsrt.2017.05.010.
URL http://dx.doi.org/10.1016/j.jqsrt.2017.05.010

[33] A. Kottke, pygmm (2020). doi:https://zenodo.org/badge/latestdoi/21452/arkottke/pygmm.
URL https://zenodo.org/badge/latestdoi/21452/arkottke/pygmm

[34] T. R. Drevon, pyScatSpheres.
URL https://pypi.org/project/pyScatSpheres/

[35] E. J. Kirkland, Advanced Computing in Electron Microscopy, third edit Edition, Springer, 2019.

[36] H. J. Müller, On the calculation of Regge trajectories in non-relativistic potential scattering, Physica 31 (5) (1965) 688–692. doi:10.1016/0031-8914(65)90006-6.